Neural network representation of electronic structure from *ab initio* molecular dynamics

Qiangqiang Gu,[1] Linfeng Zhang,[2] and Ji Feng[1,3,*]

[1] *International Center for Quantum Materials, School of Physics, Peking University, Beijing 100871, China*
[2] *Department of Mathematics and Program in Applied and Computational Mathematics, Princeton University, Princeton, NJ 08544, USA*
[3] *Collaborative Innovation Center of Quantum Matter, Beijing 100871, China*

(Dated: November 30, 2020)

Despite their rich information content, electronic structure data amassed at high volumes in *ab initio* molecular dynamics simulations are generally under-utilized. We introduce a transferable high-fidelity neural network representation of such data in the form of tight-binding Hamiltonians for crystalline materials. This predictive representation of *ab initio* electronic structure, combined with machine-learning boosted molecular dynamics, enables efficient and accurate electronic evolution and sampling. When applied to a one-dimension charge-density wave material, carbyne, we are able to compute the spectral function and optical conductivity in the canonical ensemble. The spectral functions evaluated during soliton-antisoliton pair annihilation process reveal significant renormalization of low-energy edge modes due to retarded electron-lattice coupling beyond the Born-Oppenheimer limit. The availability of an efficient and reusable surrogate model for the electronic structure dynamical system will enable calculating many interesting physical properties, paving way to previously inaccessible or challenging avenues in materials modeling.

I. INTRODUCTION

Ab initio molecular dynamics (AIMD)[1, 2] have been the mainstay for modeling materials thermodynamic and kinetic behaviors to do with atomic motions, offering concomitantly highly accurate description of electronic structures. In an AIMD simulation, a huge number of atomic configurations have to be sampled for meaningful statistics, during which the Born-Oppenheimer (BO) electronic structure as a function of atomic trajectory is evaluated at *ab initio* level. Although a number of electronic properties can be computed on-the-fly, the electronic structure data, generated at high volumes and significant computation costs, are generally under-utilized, despite exceedingly rich information in these data. This is precisely a situation where a concise and predictive representation of the *ab initio* electronic structure data to harvest the electronic information discarded after AIMD is expected to be highly rewarding. This will constitute a reusable surrogate model, which can significantly expedite the sampling of configuration-dependent electronic structure.

The above problem falls squarely in the realm of deep neural network, which has become a powerful and versatile paradigm for computerized analysis and interpretation of massive data.[3] Through supervised observation of labeled data, a neural network automatically recognizes patterns and regularities in the data and hence becomes predictive regarding the features it is devised to represent. In turn, the predictive neural network can substitute the originally time-consuming calculation with significant speed-up. For example, Neural network representation of the interatomic potential has been developed and can reproduce the atomic trajectory without time-consuming *ab initio* calculations.[4–8] In these methods, the total potential energy is decomposed into a sum of atomic energy contributions, which is represented by neural networks through the atom and its neighbors (local chemical environment). However, the electronic information available in the AIMD is entirely lost in this approach. Therefore, a predictive representation of electronic structure to pick up the rich electronic structure information in AIMD simulation is highly desirable, which will enable many previous inaccessible or challenging tasks in modeling the electronic properties of a large and dynamical system.

In this paper, we present a neural network architecture to efficiently represent the electronic structure data from AIMD simulations. This architecture will employ a deep feedforward network to process atom trajectory and band structures, to produce a representation that predicts a tight-binding Hamiltonian for a given snapshot of atomic configuration. The main challenge is that the neural network predicted tight-binding (dubbed TBworks hereafter) Hamiltonian is not uniquely determined by its band structure due to the $U(N)$ gauge freedom, which calls for much effort in designing the neural network architecture and optimization process. It is shown that by the elaborate design of the neural network architecture, the gauge freedom can be reduced. After introducing the architecture and algorithm, the method is tested using a one-dimension charge-density wave (CDW) material, carbyne. It is shown that the *ab initio* electronic structure can be faithfully reproduced by the predicted Hamiltonian. Based on the machined-learned force field, large scale molecular dynamics (MD) simulations are performed on carbyne, during which TBworks can be applied to sample the electronic structures and the derived prop-

* jfeng11@pku.edu.cn

erties. This enables us to sample the electronic states in the dynamical annihilation of a soliton-antisoliton pair to compute the time-dependent spectral function, beyond the Born-Oppenheimer approximation. Optical conductivity is also obtained by sampling the current-current correlation function in a path-integral molecular dynamics. These results suggest that our TBworks, combined with machine-learned force field, realizes a paradigm for expedited electronic structure sampling at *ab initio* accuracy, which enable capture the non-adiabatic effect in transient processes by large-scale and long-time simulations.

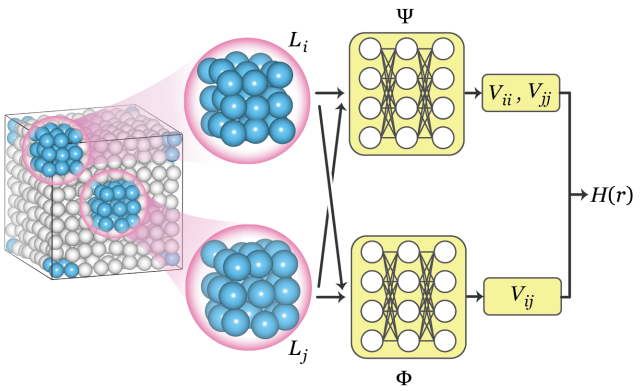

Fig. 1. Schematic of the local chemical environment construction and neural network structure. Ions in local environments L_i and L_j are depicted as blue balls enclosed by translucent spheres. Ψ and Φ are multilayer fully connected neural networks with a hyperbolic tangent activation (open circles).

II. ALGORITHM

In an *ab initio* molecular dynamics simulation, a trajectory of ion positions is generated at a discrete set of time points, $\boldsymbol{u}_i(t) = \boldsymbol{r}_i(t) - \bar{\boldsymbol{r}}_i$, where $\boldsymbol{r}_i(t)$ and $\bar{\boldsymbol{r}}_i$ are respectively the instantaneous and the reference ion positions. Periodic boundary conditions are imposed on the simulation box, such that the *ab initio* eigenstates are Bloch functions. An *ab initio* molecular dynamics yields a set of instantaneous electronic eigenstates for an ionic configuration $\boldsymbol{r} = \{\boldsymbol{r}_i\}$, with corresponding energy spectrum (bands) $\hat{\varepsilon}(\boldsymbol{r}) = \{\hat{\varepsilon}_{n\boldsymbol{k}}\}$. The aim is then to use $\boldsymbol{r}$ and $\hat{\varepsilon}(\boldsymbol{r})$ to train a neural network as a surrogate model for *ab initio* calculation, through a tight-binding electronic Hamiltonian as a function of $\boldsymbol{r}$.

$$H(\boldsymbol{r}) = \sum_{i\neq j} V_{ij}(\boldsymbol{r}) c_i^\dagger c_j + \sum_i V_{ii}(\boldsymbol{r}) c_i^\dagger c_i + \text{H.c.}, \quad (1)$$

where $V_{ij}(\boldsymbol{r})$ $(i \neq j)$ is a hopping matrix element and $V_{ii}(\boldsymbol{r})$ is the on-site energy. Assuming that there is only a single orbital on each ion for notational brevity, i and j are also site indices.

Providing the existence of Wannier functions [9–11], it suffices to keep hopping matrix elements between pairs of orbitals within a finite range. Therefore, We introduce a *local chemical environment* for each site, as shown in Fig. 1. For site i, the ions lying within a sphere of radius R_{cut} centered at $\boldsymbol{r}_i$ form its local chemical environment $L_i = \{j|\ |\boldsymbol{r}_j - \boldsymbol{r}_i| < R_{\text{cut}}\}$, which assumes non-negligible influence on the Wannier function on site i. Therefore, the hopping matrix element V_{ij} will depend on $\bar{\boldsymbol{r}}_{ij}$, $\boldsymbol{u}_i$, $\boldsymbol{u}_j$, L_i, and L_j, where $\bar{\boldsymbol{r}}_{ij} = \bar{\boldsymbol{r}}_i - \bar{\boldsymbol{r}}_j$. The on-site energy V_{ii} can be fully determined by L_i. A naïve neural network for our purpose is composed of two maps (see Fig.1): $V_{ij} = \Phi(X;\theta)$ and $V_{ii} = \Psi(Y;\xi)$, where $X = (\bar{\boldsymbol{r}}_{ij}, \boldsymbol{u}_i, \boldsymbol{u}_j, L_i, L_j)$, $Y = L_i$. θ and ξ are trainable parameters of the neural network. The tight-binding Hamiltonian $H(\bar{\boldsymbol{r}})$ for reference configuration (usually an equilibrium crystal structure) is easily accessible with standard Wannierization method,[12] which is used to calibrate the neural network in a refined architecture,

$$\begin{aligned} V_{ij} &= \bar{V}_{ij} + \Phi(X;\theta) - \Phi(\bar{X};\theta), \\ V_{ii} &= \bar{V}_{ii} + \Psi(Y;\xi) - \Psi(\bar{Y};\xi). \end{aligned} \quad (2)$$

Obviously, when $\boldsymbol{r} = \bar{\boldsymbol{r}}$, $\Phi(X;\theta) - \Phi(\bar{X};\theta)$ and $\Psi(Y;\xi) - \Psi(\bar{Y};\xi)$ equal zero for the neural network to produce exactly $H(\bar{\boldsymbol{r}})$. Although we only show the neural network maps for the cases of single orbital on each ion for brevity, generalization to multi-orbital case is straightforward by allocating individual maps for hoppings between different orbitals.

The maps Φ and Ψ are fulfilled through deep feed-forward neural networks with n hidden layers neurons, as shown in Fig.1. Take the map Φ as an example, $\Phi = \Phi_n \circ \Phi_{n-1} \circ \ldots \circ \Phi_1$. The μ-th hidden layer, Φ_μ takes the output vector of the preceding layer $x_{\mu-1}$, and generates a new vector through the component-wise hyperbolic tangent activation, $x_\mu = \tanh(w_\mu x_{\mu-1} + b_\mu)$, with $x_0 = X$, and $V_{ij} = x_n$. Here the matrix w_μ reweights $x_{\mu-1}$ and the vector b_μ provides a bias, both of which are adjustable parameters and determined via the Adam stochastic gradient descent method[13] employed to minimize the loss function during a back-propagation process. The loss function is the root-mean-square (rms) deviation between energy spectra $\varepsilon(\boldsymbol{r})$ computed from predicted $H(\boldsymbol{r})$ and training labels from the *ab initio* $\hat{\varepsilon}(\boldsymbol{r})$. In principle, $H(\boldsymbol{r})$ is not uniquely determined by energy spectra $\hat{\varepsilon}(\boldsymbol{r})$ alone due to the existence of gauge freedom. If a different gauge is chosen at different $\boldsymbol{r}$, $H(\boldsymbol{r})$ as a function of $\boldsymbol{r}$ may not necessarily be smooth and continuous. Because of the discontinuity, the predicted $H(\boldsymbol{r})$ may not interpolate well for unseen configurations, not to mention extrapolations. Fortunately, the continuity of $H(\boldsymbol{r})$ is fulfilled automatically in our neural network implementation, since the relationships between $\boldsymbol{r}$ and $H(\boldsymbol{r})$ are represented by Φ and Ψ, which are smooth and continuous composite maps. Indeed, the TBworks gives the desired performance in the test example to be discussed next.

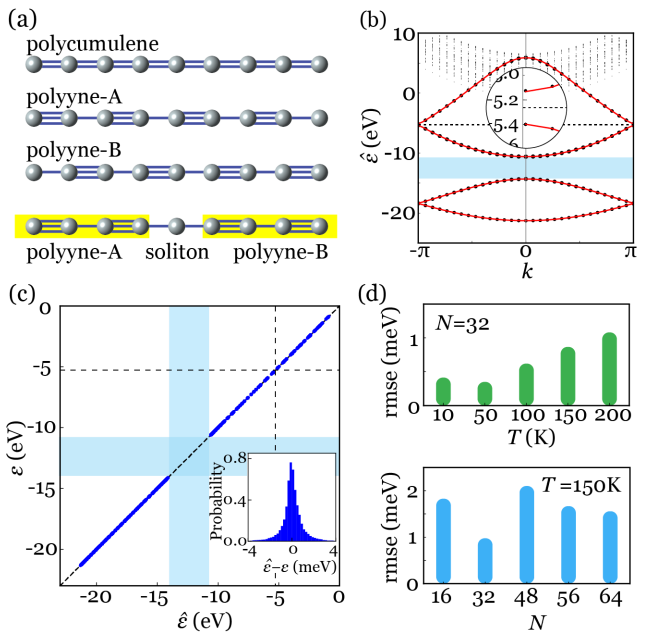

Fig. 2. Performance of neural network representation of the electronic structure of carbyne. (a) Structure of carbyne, including (from top to bottom) polycumulene, two polyynes, and a chain with a kink excitation. (b) TBworks (red line) and *ab initio* (black dots) band structure for polyyne. Blue shaped region indicates the *s*-*p* separation, and the black dashed line indicates the CDW gap (a blow-up view in the inset). (c) TBworks predicted vs *ab initio* eigenvalues for unseen snapshots with different simulation box sizes and temperatures, $T = 10, 50, 100, 150, 200$ K and $N = 16, 32, 48, 56, 64$. Inset: error distribution. (d) Generalization root-mean-square error (rmse) for unseen snapshots with a simulation box size $N = 32$ at different temperatures (upper panel) and snapshots at $T = 150$K with different simulation box sizes (lower panel).

III. METHODS

Training and testing data. The *ab initio* molecular dynamics with the canonical ensemble were performed through the Vienna *ab initio* simulation package[14] with the local density approximation[15]. Nose-Hoover thermostat[16, 17] was used to maintain the temperatures. The cutoff energy is 400 eV for wave functions expansion in the plane wave basis sets. The AIMD simulations were performed with the simulation box sizes containing $N = 16$, 32, 48, 56 and 64 C atoms. For each box, we have sampled its trajectory at the canonical ensembles for temperature $T = 10$, 50, 100, 150, and 200 K. The eigenvalue labels are calculated using $1 \times 1 \times 4$ and $1 \times 1 \times 2$ k-mesh for $N = 16$ and $N = 32$ boxes, while for box size larger than 32 cases, only Γ point was used. We use the labeled AIMD data of 5000 snapshots from one of the trajectories with $N = 32$ at $T = 150$ K as the training data. In order to test the generalization and transferability of our method, the labeled AIMD data from 5000 snapshots for every unlearned trajectories sampled at different temperatures and system sizes are set as testing data.

Machined-learned molecular dynamics. Path-integrals molecular dynamics (PIMD) and classical molecular dynamics (CMD) were performed by the LAMMPS package[18] with the Machined-learned force fields generated by DeePMD-kit package.[19] The Nose-Hoover[16, 17] and Nose-Hoover massive chain[20] thermostats are applied in CMD and PIMD respectively to maintain the temperatures in the canonical ensemble. The time step is set to 0.2 femtoseconds for both CMD and PIMD. The quantum paths are discretized into 12 imaginary time slices in the PIMD. The deep nneural network for force field was set to be [200,200,200] and was trained by AIMD data from 10000 snapshots. Validation data contains AIMD data from 1000 snapshots. More details about the setup parameters will be available upon request. The testing accuracy for force prediction is up to 0.01 eV/Å and for total energy prediction is 10^{-5} eV, which is at the same level of the *ab initio* calculation.

IV. PERFORMANCE

We now proceed to evaluate the performance of our neural network algorithm by learning and then predicting AIMD eigenvalues for a charge-density wave material, carbyne.[21–23] Carbyne is a one-dimensional sp^1 hybridized carbon chain, which can undergo an archetypal Peierls' transition[24] from polycumulene (=C=C=) to polyyne (−C≡C−). Polyyne has two degenerate ground state structures interrelated by a shift of the single and triple bonds, as shown in Fig.2(a). Polyyne can be characterized by the order parameter $u_\alpha = (-1)^\alpha u_0$ ($\alpha = 1, 2, \cdots, N$), and sign(u_0) $= \pm 1$ corresponds to the two degenerate phases. Remarkably, sign(u_0) $= \pm 1$ can coexist on a single carbyne chain, separated by a domain wall or a kink in u_α, which can lead to solitonic excitations.[25] Bond ordering and solitonic excitations make carbyne an interesting and non-trivial material for testing our algorithm.

In carbyne, the C-C σ bonds are formed by the overlap of sp^1 hybridized orbitals while the π bonds are formed by the other two half-filled p orbitals perpendicular to the carbon chain. The s and p bands within the energy window (-22 – 0 eV) are picked out as label data from 5000 AIMD snapshots of $N = 32$ C atoms at $T = 150$ K to train the TBworks. Fig.2(b) displays a faithful reproduction of the band structure of polyyne by the trained TBworks, including the charge-density wave gap $\Delta \sim 27$ meV. The reproduction of band structures for more structures can be seen in the Fig.S1 in supplementary materials. In Fig.2(c), the TBworks predicted spectra for snapshots unseen in training are plotted against *ab initio* spectra, where samples are drawn from AIMD with multiple temperatures (10 – 200 K) and a range of sim-

ulation box sizes. The generalization error (rms deviation) of these predictions is ~ 1 meV and the coefficient of determination $R^2 = 0.99999994$. The s-p separation of ~ 3.72 eV and the CDW gap ~ 27 meV are also well reproduced despite their disparate energy scales. As is also shown in Fig.2(d), the generalization error of the TBworks trained at a single T and N are on the order of 1 meV, when tested against data from multiple temperatures and simulation box sizes. Therefore, we conclude that the TBworks trained at a single T and N offers a faithful representation of the *ab initio* electronic structure, which is also highly transferable to a range of temperatures and system sizes unseen in the initial learning.

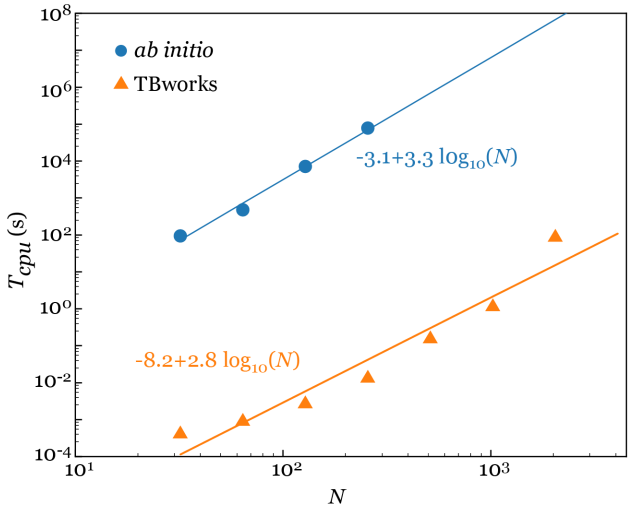

Fig. 3. Compute time T_{cpu} for calculating the electronic spectra of carbyne vs system size N in *ab initio* and TBworks calculations. Here T_{cpu} is the CPU time on a compute node equiped with 2 AMD EPYC-7452 CPUs (64 cores). The *ab initio* calculation is performed at Γ point[14], with plane-wave basis cutoff at 400 eV and total energy convergenece to within 10^{-4} eV per atom. The dots (*ab initio*) and triangles (TBworks) mark the computation costs for different N. The solid lines are the least-square linear fittings between variable $\log_{10}(T_{cpu})$ and $\log_{10}(N)$.

With the accuracy perfectly preserved, we further investigate the efficiency of the TBworks model. As shown in Fig.3, due to the inevitable diagonalization procedure, the computation cost of both the TBworks and *ab initio* calculations scale roughly as $\sim N^3$, where N denotes the system size. However, the prefactor is different by more than 5 orders of magnitude. This is because in *ab initio* calculations, diagonalization happens in solving the Kohn-Sham equations[26], where the one-electron wave functions are expanded over a large basis set of size proportional to but way larger than N; while in TBworks, the size of the Hamiltonian is the number of Wannier orbitals, which is generally of the same order of N. As such, the dramatic speed-up in TBworks makes the accessible system size around 2 orders of magnitude larger than *ab initio* calculations.

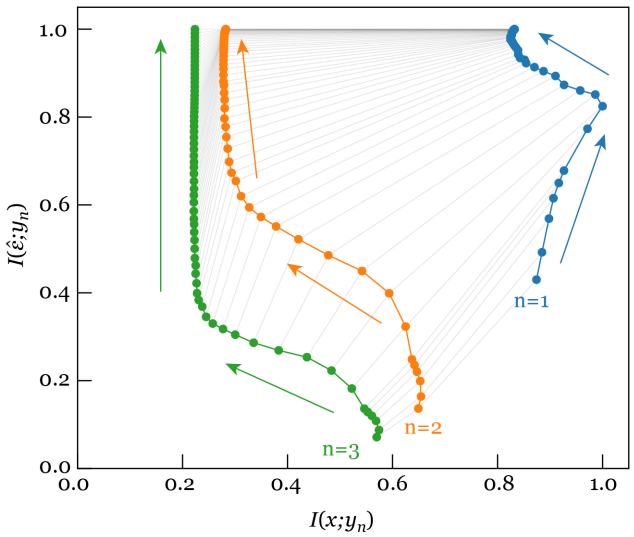

Fig. 4. Information plane loci of a 3-layer TBworks during training, showing the mutual information trajectories of a [200, 200, 200] neural network in 800 epoches. The colored solid arrows are guide-of-eye indications of the direction of progression for the three loci.

Further insights into the performance of the TBworks are gained by visualizing the training process on a reduced information plane.[27, 28] The mutual information $I(a;b)$ is an asymmetric measure of the correlation between a pair of random variables a and b, with distributions $P(a)$ and $P(b)$, respectively,

$$I(a;b) = D_{\mathrm{KL}}(P(a,b)||P(a)\otimes P(b)) \qquad (3)$$

where D_{KL} is the Kullback-Leibler divergence and $P(a,b)$ is the joint distribution.[29] We compute the mutual information between the input x (ionic coordinates inside a simulation box) and the output of the n-th layer y_n, and the mutual information between the training label $\hat{\varepsilon}$ and the output y_n. Thus we can visualize the evolution of the neural network on the reduced information plane $I(x,y_n)$-$I(\hat{\varepsilon},y_n)$, as depicted in Fig.4. We see that $I(\hat{\varepsilon},y_1)$ undergoes a continuous sharp increase throughout the training, which directly results from the optimization of the loss function, indicating continued improvement of model fitting. $I(x,y_1)$ increases slightly then decreases in the later stage. The decrease in $I(x,y_1)$ is a manifestation of reduction of data redundancy, which is very important for the performance of the neural network. The dynamics of layers 2 and 3 are also bi-phasic, where redundancy elimination precedes the rapid model improvement. The redundant information on x arises from a large cut-off radius R_{cut} for the local chemical environment, which includes atoms having little impact on the hopping amplitude. Therefore, the information plane analysis uncovers critical stages in the learning process

of neural network during the training process, and offers leads for systematically optimizing the choice of setup parameter for TBworks.

V. APPLICATION

The efficient, accurate and transferable access to $H(\boldsymbol{r})$ offered by our TBworks provides a convenient computational tool for investigating the correlation between electronic and ionic degrees of freedom, which is particularly important for systems with strong electron-phonon coupling. The soliton-antisoliton pair annihilation process is one such example, where the zero-energy electronic modes are gapped out dynamically. Non-adiabatic effect can be important but difficult to study in AIMD due to the high demand for computational resources. In order to study this kind of process, we interface our TBworks with the machine-learned force field[8] to perform highly efficient classical and path-integral MD on carbyne. Both the classical and path-integral MD simulations were performed in the canonical ensemble on a supercell containing 1024 C atoms for 400 picoseconds (ps) with a time step of 0.2 femtoseconds (fs) at different temperatures. The simulation results including the averaged electronic spectral functions and optical conductivities are reported in Fig.S3 in the supplementary materials. Fig.5(a) shows the order parameters u_α of the ionic configurations in the dynamical process where soliton-antisoliton pair is annihilated from the classical MD trajectory initialized with soliton structure at $T = 1$ K.

To highlight the non-adiabatic dynamical effect in the soliton-antisoliton pair annihilation, we take a close look at the time-dependent electronic spectral functions. Because of the quick access to TBworks Hamiltonian, we are able to let the electronic system evolve according to $\mathcal{T}e^{-\mathrm{i}\int_{t_0}^{t} H\left(r(t')\right)dt'}$ ($\hbar = 1$). Doing so explicitly takes ion dynamics into account and is manifestly beyond the BO approximation. As ion dynamics breaks time homogeneity for electrons, we define a time-dependent spectral function as

$$A(\omega, t) = \frac{\mathrm{i}}{2\pi N}\hat{F}\,\mathrm{Tr}\left[G^R(t+\tau, t) - G^A(t+\tau, t)\right] \quad (4)$$

where $G^{A/R}_{\alpha\beta}(t+\tau, t) = \pm\mathrm{i}\,\theta(\mp\tau)\langle\{c_\alpha(t+\tau), c^\dagger_\beta(t)\}\rangle$ are advanced/retarded Green's functions, and $\hat{F}$ means a Fourier transform w.r.t. the time difference τ.[30] At different t, the advanced and retarded Green's functions are evaluated by computing the expectation of the commutator $\{c_\alpha(t+\tau), c^\dagger_\beta(t)\}$ for $\tau > 0$ ($G^R_{\alpha\beta}(t+\tau, t)$) and $\tau < 0$ ($G^A_{\alpha\beta}(t+\tau, t)$) respectively. The τ-values are taken from a uniform grid ranging from -600 to 600 fs, which, after a Fourier transform, results in the the energy resolution in $A(\omega, t)$ of ~ 3 meV, 0.1 of the CDW gap. At each τ, the electronic evolution of the operator $c_\alpha(t)$ from t to $t+\tau$ is calculated based on the Schrödinger equation using $\mathcal{T}e^{-\mathrm{i}\int_{t}^{t+\tau} H\left(r(t')\right)dt'}$, where the time-dependent Hamiltonian is predicted for the configurations from the trajectory at t to $t+\tau$. Therefore, the $A(\omega, t)$ can be non-adiabatically calculated along the evolution of configurations $\boldsymbol{r}(t)$ in the MD simulation. As a comparison, the static electronic spectral function within the BO approximation for configuration at t is calculated using instantaneous energy spectra, with $A_{\mathrm{stat}}(\omega, t) = \frac{1}{N_k}\sum_{nk}\delta(\omega - \varepsilon_{nk}(t))$.

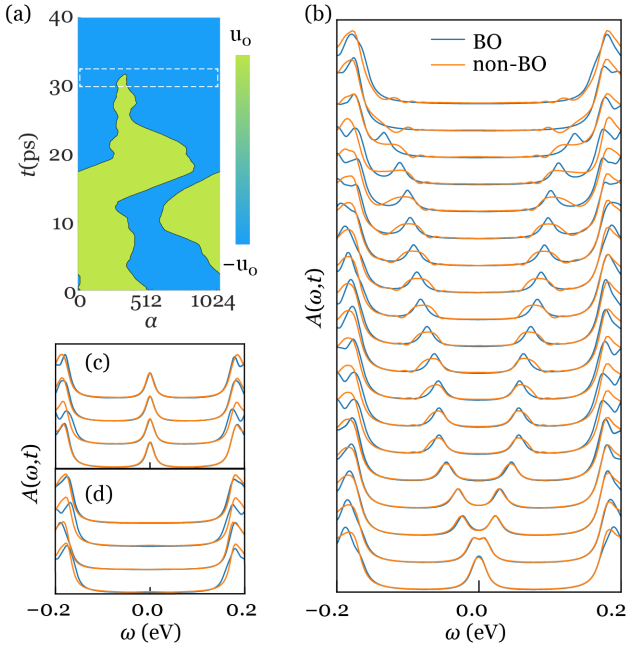

Fig. 5. Non-adiabatic dynamical effect on the electronic spectral functions during the soliton-antisoliton pair annihilation process. (a) The order parameter along a polyyne chain as a function of time in a molecular dynamics trajectory. The dashed rectangle indicated the soliton-antisoliton pair annihilation event. (b) Computed time-dependent electronic spectral functions for structures at every 20 fs in the annihilation event. (c)(d) Computed electronic spectral functions for structures before (c) and after (d) annihilation event.

We therefore focus on the soliton-antisoliton pair annihilation event indicated by the dashed rectangle in Fig.5(a). During this event, two kinks meet and annihilate, and the polyyne-B phase completely disappears. At the same time, the degenerate zero-energy modes localized at the kinks become hybridized and a gap gradually develops. The question is whether the BO approximation is accurate enough to describe the electronic states for the dynamical annihilation process. As a comparison, we firstly examined the electronic spectral functions for structures well before (Fig.5(c)) and after (Fig.5(d)) the annihilation event. Prior to the annihilation event where the soliton and anti-soliton are well separated, both dynamical (beyond BO approximation) and static (within BO approximation) spectral functions give the same topological protected zero-energy peaks, as shown

in Fig.5(c), where little difference between the dynamical and static spectral functions is discernible. Post annihilation, the carbyne chain adopts a homogeneous polyyne-A structure, where both dynamical and static spectral functions present the CDW gap, as shown in Fig.5(d). Again, little difference between the dynamical and static spectral functions is uncovered, because the system is in a (transient) stationary state. For the case during this annihilation event, the dynamical and static time-dependent spectral functions for the annihilation process are calculated and shown in Fig.5(b). Both dynamical and static spectral functions show the splitting of the zero-energy modes into two peaks, which subsequently merge into the conduction and valence bands respectively as the soliton-antisoliton pair approaching to annihilation. The difference is that the energy peaks in the dynamical spectral functions show a larger broadening than those in the static spectral functions. In short, although the dynamical effect shows little renormalization on the spectral functions before and after the annihilation event, as far as the pair annihilation process is concerned, the non-adiabatic dynamical effect is prominently visible in our calculations.

VI. SUMMARY

In this work, we have developed a neural network-based predictive representation method, which predicts tight-binding Hamiltonians for modeling electronic structures. This method provides an efficient approach to configuration-dependent Hamiltonians by directly supervised observation of the *ab initio* energy spectra. This enables an expedited access to electronic structures at dramatically reduced computational costs during the atomic configurations sampling, in subsequent molecular dynamics or Monte Carlo. Considering the example of carbyne, we demonstrate the accuracy of our method in predicting the electronic spectra is comparable to that of the *ab initio* calculations. The TBworks also shows a high degree of transferability, accurately predicting spectra for configurations drawn from unseen temperatures and system sizes.

By interfacing our TBworks with a machined-learned force field it is demonstrated that we can efficiently sample the electronic structure of carbyne in molecular dynamics to compute correlation functions. This enables the computation of Green's functions and the time-dependent spectral functions in the dynamical annihilation of a soliton-antisoliton pair. When compare our results with those from the adiabatic approximation, it is found that the low-energy edge modes is significant renormalized due to the non-adiabatic dynamical effect. We have also applied the TBworks sampling of electronic structure in a path-integral molecular dynamics, where the optical conductivity is computed by sampling the current-current correlation function. These results suggest that our method provides an efficient and accurate computation tool for sampling electronic structure in order to compute correlation functions and associated physical properties. The low computational cost and dramatic speed-up of a combined machine-learned force field and TBworks for such purposes as compared shall enable large-scale and long-time simulation, and as we have demonstrated, capturing non-adiabatic effect in transient processes.

ACKNOWLEDGMENTS

This work is supported by the National Natural Science Foundation of China (Grant No. 11725415 and No. 11934001), the Ministry of Science and Technology of the People's Republic of China (Grant No. 2018YFA0305601 and No. 2016YFA0301004), and by the Strategic Priority Research Program of Chinese Academy of Science (Grant No. XDB28000000). The work of L. Z. is supported in part by the Center Chemistry in Solution and at Interfaces (CSI), Princeton, funded by the DOE Award DE-SC0019394.

[1] R. Car and M. Parrinello, Unified approach for molecular dynamics and density-functional theory, Phys. Rev. Lett. **55**, 2471 (1985).
[2] D. Marx and J. Hutter, *Ab Initio Molecular Dynamics: Basic Theory and Advanced Methods* (Cambridge Univ. Press, 2009).
[3] Y. LeCun, Y. Bengio, and G. Hinton, Deep learning, Nature **521**, 436 (2015).
[4] J. Behler and M. Parrinello, Generalized neural-network representation of high-dimensional potential-energy surfaces, Phys. Rev. Lett. **98**, 146401 (2007).
[5] K. T. Schütt, F. Arbabzadah, S. Chmiela, K. R. Müller, and A. Tkatchenko, Quantum-chemical insights from deep tensor neural networks, Nat. Commun. **8**, 13890 (2017).
[6] J. S. Smith, O. Isayev, and A. E. Roitberg, ANI-1: an extensible neural network potential with DFT accuracy at force field computational cost, Chem. Sci. **8**, 3192 (2017).
[7] L. Zhang, J. Han, H. Wang, R. Car, and W. E, Deep potential molecular dynamics: A scalable model with the accuracy of quantum mechanics, Phys. Rev. Lett. **120**, 143001 (2018).
[8] L. Zhang, J. Han, H. Wang, W. Saidi, R. Car, and W. E, End-to-end symmetry preserving inter-atomic potential energy model for finite and extended systems, Adv. Neural Inf. Process. Syst. **32**, 4436 (2018).
[9] C. Brouder, G. Panati, M. Calandra, C. Mourougane, and N. Marzari, Exponential localization of wannier functions in insulators, Phys. Rev. Lett. **98**, 046402 (2007).
[10] J. D. Cloizeaux, Analytical properties of n-dimensional

energy bands and wannier functions, Phys. Rev. **135**, A698 (1964).
[11] G. Nenciu, Existence of the exponentially localised wannier functions, Comm. Math. Phys. **91**, 81 (1983).
[12] N. Marzari, A. A. Mostofi, J. R. Yates, I. Souza, and D. Vanderbilt, Maximally localized wannier functions: Theory and applications, Rev. Mod. Phys. **84**, 1419 (2012).
[13] D. P. Kingma and J. Ba, Adam: A method for stochastic optimization, arXiv preprint arXiv:1412.6980 (2014).
[14] G. Kresse and J. Furthmüller, Efficient iterative schemes for ab initio total-energy calculations using a plane-wave basis set, Phys. Rev. B **54**, 11169 (1996).
[15] J. P. Perdew and A. Zunger, Self-interaction correction to density-functional approximations for many-electron systems, Phys. Rev. B **23**, 5048 (1981).
[16] S. Nosé, A molecular dynamics method for simulations in the canonical ensemble, Mol. Phys. **52**, 255 (1984).
[17] W. G. Hoover, Canonical dynamics: Equilibrium phase-space distributions, Phys. Rev. A **31**, 1695 (1985).
[18] S. Plimpton, Fast parallel algorithms for short-range molecular dynamics, J. Comput. Phys. **117**, 1 (1995).
[19] H. Wang, L. Zhang, J. Han, and W. E, Deepmd-kit: A deep learning package for many-body potential energy representation and molecular dynamics, Comput. Phys. Commun. **228**, 178 (2018).
[20] M. E. Tuckerman, B. J. Berne, G. J. Martyna, and M. L. Klein, Efficient molecular dynamics and hybrid monte carlo algorithms for path integrals, J. Chem. Phys. **99**, 2796 (1993).
[21] R. B. Heimann, J. Kleiman, and N. M. Salansky, A unified structural approach to linear carbon polytypes, Nature **306**, 164 (1983).
[22] C. Jin, H. Lan, L. Peng, K. Suenaga, and S. Iijima, Deriving carbon atomic chains from graphene, Phys. Rev. Lett. **102**, 205501 (2009).
[23] O. Cretu, A. R. Botello-Mendez, I. Janowska, C. Pham-Huu, J.-C. Charlier, and F. Banhart, Electrical transport measured in atomic carbon chains, Nano Lett. **13**, 3487 (2013).
[24] M. Kertesz, J. Koller, and A. Azman, Ab initio hartree–fock crystal orbital studies. ii. energy bands of an infinite carbon chain, J. Chem. Phys. **68**, 2779 (1978).
[25] W. P. Su, J. R. Schrieffer, and A. J. Heeger, Solitons in polyacetylene, Phys. Rev. Lett. **42**, 1698 (1979).
[26] W. Kohn and L. J. Sham, Self-consistent equations including exchange and correlation effects, Phys. Rev. **140**, A1133 (1965).
[27] N. Tishby and N. Zaslavsky, Deep learning and the information bottleneck principle, in *2015 IEEE Information Theory Workshop (ITW)* (2015) pp. 1–5.
[28] R. Shwartz-Ziv and N. Tishby, Opening the black box of deep neural networks via information, arXiv preprint arXiv:1703.00810 (2017).
[29] S. Kullback and R. A. Leibler, On information and sufficiency, Ann. Math. Statist. **22**, 79 (1951).
[30] H. T. M. Nghiem and T. A. Costi, Time evolution of the kondo resonance in response to a quench, Phys. Rev. Lett. **119**, 156601 (2017).

Appendix A: Predicted v.s. *ab initio* band structure

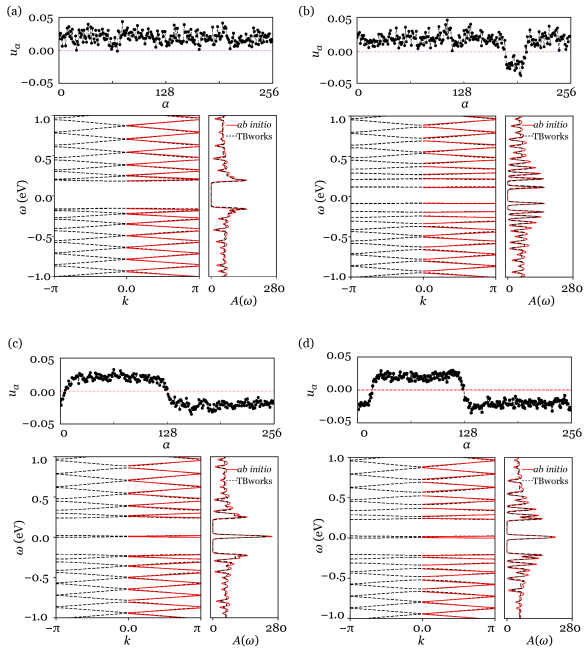

Fig. 6. Comparison between TBworks predicted and *ab initio* calculated electronic structure. The crystal configurations are randomly picked snapshots from the molecular dynamics (MD) trajectory on a supercell containing $N = 256$ C atoms. The upper panel of each subplot is the order parameter which indicates the polyyne (a) and soliton phase (b-d). The predicted band structures and the corresponding density of states $A(\omega)$ show great consistency with the *ab initio* ones.

Appendix B: Energy barrier between polyyne and soliton phase

As illustrated in Fig.7(a), there are two kinds of transition paths for polyyne to soliton structure. Fig.7(b) shows the direct transition barriers from polyyne to the soliton structures with different separation between soliton-antisoliton pair. The results show that the larger separation comes with the higher transition barrier. Therefore, the reasonable transition path should be the indirect path, whose potential profile is shown in Fig.7(c). The soliton-antisoliton pair with small separation is generated from polyyne structure with the energy barrier ~ 80 meV and then solitons move freely along the chain to generate the structure with large separated soliton-antisoliton pair. The uneven potential profile in Fig.7(c) indicates that annihilation for soliton-antisoliton pair is much easier than formation. Therefore, at low temperature, classical MD can only sample the ground states polyyne structure. While in path-integral MD, due to the quantum tunneling, the soliton phase can be sam-

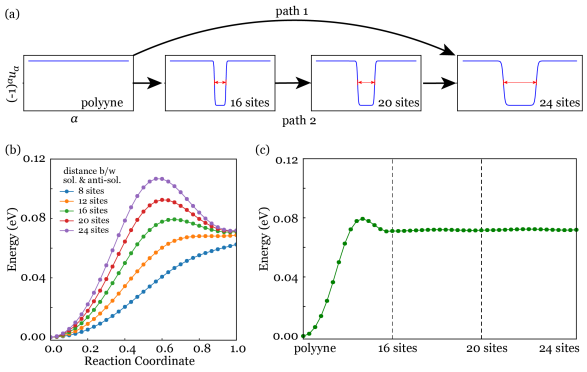

Fig. 7. Energy barrier for the transition between polyyne and soliton structure. (a) Direct and indirect transition paths between polyyne and soliton structure with the soliton and anti-soliton separated by 24 sites. (b) Direct transition barrier for the transition between polyyne structure and soliton structure with different separation between soliton and anti-soliton.(c) Indirect transition barrier for the transition path 2 in (a).

pled at low temperature.

Appendix C: Electronic spectral function and optical conductivity.

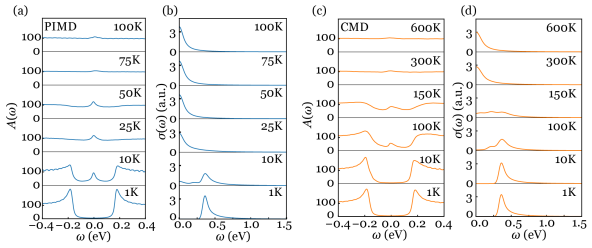

Fig. 8. The averaged electronic spectral function $A(\omega)$ and optical conductivity $\sigma(\omega)$ for supercell $N = 1024$ at different temperatures. Electronic spectral function (a) and optical conductivity (b) averaged in the canonical ensemble sampled by path-integral molecular dynamics (PIMD). Electronic spectral function (c) and optical conductivity (d) averaged in the canonical ensemble sampled by classical molecular dynamics (CMD).

In addition to the research on the dynamical electronic evolution in the soliton-antisoliton pair annihilation process shown in main text, the averaged electronic spectral function and optical conductivity are calculated in the canonical ensemble sampled by machined-learned force field path-integral and classical molecular dynamics. The MD is performed with the simulation box size $N = 1024$ C atoms for 400 ps with a time step of 0.2 fs at different temperatures. The spectral function and optical conductivity are averaged using ionic configurations sampled by MD, $A(\omega) = \mathrm{Tr}\{\rho(\boldsymbol{r})A(\omega,t)\}$ and $\sigma(\omega) = \mathrm{Tr}\left\{\rho(\boldsymbol{r})\frac{1}{\omega}\int_0^\infty e^{\mathrm{i}\omega t'}\langle[J(t'),J(0)]\rangle_{\boldsymbol{r}}dt'\right\}$, where density matrix $\rho(\boldsymbol{r})$ corresponds to the ionic degree of freedom and is obtained by MD sampling and $\langle\cdots\rangle_{\boldsymbol{r}}$ means taking the expection under the electronic states of configuration $\boldsymbol{r}$. The results are shown in Fig.8. We can see that at $T = 1$ K, the systems are in polyyne phase with a band gap $\Delta \sim 27$ meV in both path-integral and classical simulations. The optical conductivity shows a on-set at energy $\omega = \Delta$ at this temperature. As the temperature rises to 10 K, the spectral function remains the gapped feature in the CMD sampling, indicating no creation of soliton. While at the same temperature, the soliton-antisoliton pair is generated in the PIMD sampling, where the zero energy peaks in the spectral function and three peaks in optical conductivity show up. This difference in PIMD and CMD can be explained by the potential energy profile in Fig.7, which shows the transition energy barrier is ~ 80 meV from the ground state polyyne structure to soliton structure. Therefore, at low temperature, soliton structure can not be sampled for classical molecular dynamics. However, in path-integral simulation with quantum dynamical effect taken into account, the creation of soliton-antisoliton pair can be observed. As temperature goes higher to 100 K, the electronic spectral function shows neither the CDW gap nor the zero energy mode, which implys the ioninc structures are in polycumulene phase in PIMD sampling. At the same temperature, the zero energy peaks in spectral function indicate the creation of soliton in classical sampling and finally at temperature above 300 K, the classical sampling gives the polycumulene equilibrium structure. In summary, the carbyne show a sequence of phase transition from polyyne to soliton and finally polycumulene in both CMD and PIMD sampling. The difference is that due to the quantum dynamical effect, the soliton and polycumulene phase transitions happen at lower temperatures in PIMD than that in CMD. All these results exhibit the fascinating efficiency of our TBworks method that supports for investigating the electronic structures for the large scale and long time simulations.